Threshold collision induced dissociation of protonated water clusters

Sébastien Zamith, Ali Kassem, Jean-Marc L'Hermite, Christine Joblin, Jérôme Cuny

Threshold Collision Induced Dissociation of Protonated Water clusters

Sébastien Zamith,[1, a)] Ali Kassem,[1] Jean-Marc L'Hermite,[1] Christine Joblin,[2] and Jérôme Cuny[3]

[1)] *Laboratoire Collisions Agrégats Réactivité (LCAR/FERMI), UMR5589, Université Toulouse III - Paul Sabatier, CNRS, 118 Route de Narbonne, F-31062 Toulouse, France*

[2)] *Institut de Recherche en Astrophysique et Planétologie (IRAP), UMR5277, Université Toulouse III - Paul Sabatier, CNRS, CNES, 9 avenue du Colonel Roche, F-31028 Toulouse, France*

[3)] *Laboratoire de Chimie et Physique Quantiques LCPQ/FERMI, Université Toulouse III - Paul Sabatier, CNRS, 118 Route de Narbonne, F-31062 Toulouse, France*

(Dated: 26 September 2023)

We report threshold collision induced dissociation experiments on protonated water clusters thermalized at low temperature for sizes n = 19–23. Fragmentation cross sections are recorded as a function of the collision energy and analyzed with a statistical model. This model allows us to account for dissociation cascades and provides values for the dissociation energies of each cluster. These values, averaging around 0.47 eV, are in good agreement with theoretical predictions at various levels of theory. Furthermore, the dissociation energies show a trend for the n=21 magic and n=22 anti-magic numbers relative to their neighbours, which is also in agreement with theory. These results provide further evidence to resolve the disagreement between previously published experimental values. A careful quantitative treatment of cascade dissociation in this model introduces interdependence between the dissociation energies of neighboring sizes, which reduces the number of free fitting parameters and improves both reliability and uncertainties on absolute dissociation energies deduced from experiments.

[a)] Electronic mail: sebastien.zamith@irsamc.ups-tlse.fr

I. INTRODUCTION

Protonated water clusters have motivated a large number of experimental and theoretical studies due to their importance in various fields. Above all, they are good models for understanding ion induced chemistry in water.[1] In this context, proton hydration is of primary importance, and protonated water clusters offer the opportunity to study this property in detail by varying, among other parameters, the size of the system. In addition, understanding these intermediate-sized species and their microscopic properties should enable us to better understand bulk water, in particular the role of the H_3O^+ ion in the condensed phase. The development of theoretical models for water also depends on our ability to accurately describe the properties of these species for which theoretical and experimental data can be compared in a simpler way than in the condensed phase. As the H-bond network in water is essential for determining its properties, much effort has been devoted to describing it correctly. Protonated water clusters have been widely studied in this context, as they are easy to produce and manipulate for spectroscopic studies. Finally, protonated water clusters are also being studied *per se* as they are commonly encountered in various environments such as the earth's atmosphere.[2]

The structures of medium-sized protonated water clusters were determined by infrared spectroscopy.[3–6] Structural transitions as a function of cluster size have also been studied by cryogenic ion mobility mass spectrometry.[7] It appears that protonated water clusters evolve from linear to 2D (at n$\sim$10), and then to 3D structures as the size grows above n$\sim$19.[3,7] The most striking feature of this evolution, apart from the 2D to 3D transition, is the presence of a magic number at size n=21. This magic size has been known for a long time and manifests itself by its relatively high abundance compared to its neighbours in mass spectrometry.[8–18] The lowest-energy isomer of $(H_2O)_{21}H^+$ is a distorted pentagonal dodecahedron (5^{12}) with a water molecule inside.[3,4,19–23] Conversely, due to its relatively low abundance in the mass spectra, the n=22 size has been proposed as an "anti-magic" cluster. Another important issue when considering the structures of protonated water clusters is their Eigen- or Zundel-like character, i.e. the local configuration of the excess proton and its position. This property can be probed experimentally, theoretically or combining both. The position of the excess proton in $(H_2O)_{21}H^+$ has been difficult to establish considering experimental measurements only.[3,4,24] However, combined analysis with theoretical calculations led to favour the proton

being located at the surface of the cage displaying an Eigen-like character.[20,25] It is worth mentioning that this property is quite sensitive to finite-temperature effects and experimental conditions,[20,26] and that the co-existence of several structural isomers can occur as highlighted by Wu and co-workers.[20] To further understand the structure of these species, nanocalorimetric studies have also been carried out and have provided complementary information around the size n=21: disordered (liquid-like) structures have been deduced for sizes n=20, 22 and 23, while size n=21 shows a more structured behaviour.[26,27] In this context, the temperature dependence of H migration for size n=21 was also investigated.[28] The magic and anti-magic characters of sizes n=21 and n=22 were also characterised by blackbody radiation-induced fragmentation.[29]

Not only structural properties are of interest but also the energetics. Thus, the dissociation energies of protonated water clusters have also been characterized experimentally[15,17,18,30] using quite different methods. The results of these studies, summarized in Figure 1, exhibit some discrepancies around the magic size n=21.

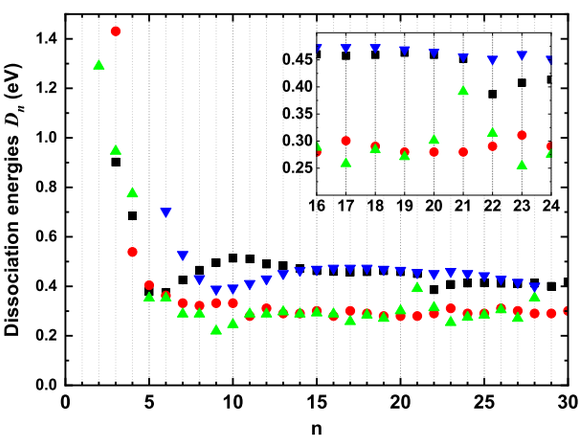

FIG. 1. Dissociation energies of protonated water clusters as a function of the cluster size from previous experimental studies. Black squares: K. Hansen *et al.*, Ref. 18. Red circles: Bruzzie *et al.*, Ref. 30. Green triangles: Magnera *et al.*, Ref. 15. Blue triangles: Shi *et al.*, Ref. 17. The inset displays the dissociation energies around the magic size n=21.

Magnera *et al.* performed Collision Induced Dissociation (CID) experiments to extract dissociation energies.[15] Shi *et al.* measured the decay fractions of the metastable clusters and used Klot's evaporative ensemble theory to deduce dissociation energies.[17] Hansen

extracted activation energies for evaporation from the relative abundances of time-of-flight mass spectra.[18] Finally, Bruzzie *et al.* obtained dissociation energies from the average kinetic energy release following evaporation.[30] Among these four studies, the most direct measurement was made by Magnera *et al.* using CID. However, their analysis does not include kinetic shifts, which is of primary importance for such experiments to be fully reliable.[31] Considering the other three studies, determination of dissociation energies is more indirect. Indeed, free decay of relatively hot clusters was considered, and dissociation energies are extracted using statistical dissociation theories.

Considering the different set of data in the size range n=16-24, we observe that Bruzzie *et al.* and Magnera *et al.* deduced similar dissociation energies, with values around 0.3 eV. In contrast, Hansen *et al.* and Shi *et al.* agree well with values around 0.45 eV. This shows that there are quite large discrepancies between the reported dissociation energies. Furthermore, none of these energies agree on the behaviour around the magic size n=21. The different data sets show either the same monotonic evolution (Bruzzie *et al.* and Shi *et al.*) but significant disagreement on the values or completely different behaviour. Hansen *et al.* measured a plateau up to size n=21, with lower values at larger sizes, attributed to a shell closure effect. In contrast, Magnera *et al.* measured an increase in dissociation energy for n=21, while neighboring sizes show a relatively constant value.

The discrepancies observed in the various experiments call for new evidence concerning these systems. Here we present measurements of the dissociation of protonated water clusters thermalized at low temperature using Threshold Collision Induced Dissociation (TCID)[31,32]. TCID is one of the most direct methods for measuring dissociation energies. In TCID, internal energy is brought to the system under study by collisions. By varying the collision energy beyond a given threshold, we observe the appearance of fragmentation channels, which are considered to result from statistical dissociation. Dissociation energies can be extracted from this threshold; the reliability of the results depends essentially on the quality of the statistical model used. In the present study, statistical dissociation is treated using Phase Space Theory (PST). The use of PST requires knowledge of certain parameters, such as the frequencies of the vibrational modes. These are obtained from self-consistent-charge density functional based tight-binding (SCC-DFTB) calculations.[33–35] We compare the dissociation energies of protonated water clusters in the n=19-23 size range with previous experimental studies and with calculations performed at the DFT, SCC-DFTB and MP2

levels. The results obtained give dissociation energies around 0.47 eV with the right trend for the magic and anti-magic numbers relative to their neighbours, as predicted by theory.

The paper is organised as follows. Section II presents the experimental methods, while the theoretical ones are exposed in section III. The main section of the paper, section IV, presents the TCID experimental results and the modeling used to extract dissociation energies. Our findings are discussed in section V. Finally, conclusions are drawn in section VI.

II. EXPERIMENTAL METHODS

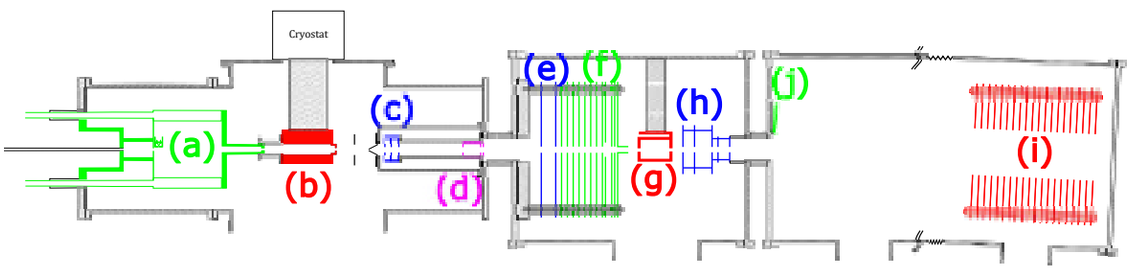

FIG. 2. Schematic view of the experimental setup. (a) Cluster gas aggregation source. (b) Thermalization chamber. (c) First Wiley-McLaren acceleration stage. (d) Mass filter. (e) Energy focusing. (f) Deceleration. (g) Collision cell. (h) Second Wiley-McLaren acceleration stage. (i) Reflectron. (j) Microchannel plate detector.

The experimental setup, which has already been described in details in previous publications[36–38], is presented here only briefly. It is depicted in Figure 2. Protonated water clusters are produced in a gas aggregation source (a) by introducing a small amount of water vapour into the helium carrier gas. This mixture is introduced into the gas aggregation source, which consists in a double-walled cylinder cooled down by a liquid nitrogen circulation. In the source, water condenses to form clusters. A corona discharge in the source gives rise to the formation of charged species. Positively charged water clusters are formed with an excess proton carrying the charge.

Once formed, the clusters are transported by the helium flow to the thermalization chamber (b). The thermalization chamber consists in a 11.3 cm long, 2 cm inner diameter copper piece attached to a closed-cycle helium cryostat. The estimated helium pressure in this chamber is about 1 mbar. Given the helium flux of 5 mbar.l.s^{-1}, the clusters take about

77 ms to travel through the thermalization chamber. Assuming a collision cross-section of 50 Å^2 between the clusters and the helium atoms, the estimated number of collisions with the helium buffer gas is of the order of 10^6. This large number of collisions brings the clusters to thermal equilibrium with the helium carrier gas. The latter is itself in thermal equilibrium with the thermalization chamber, maintained at 25 K. At this point, protonated water clusters thermalized at 25 K are therefore available. The clusters exit the thermalization chamber, whose exit diameter is 7 mm, in an effusive beam.

These clusters then enter the high-vacuum part of the experiment through a 1 mm diameter skimmer, where pulsed high voltages at a repetition rate of 800 Hz are applied to a first Wiley-McLaren acceleration stage (c). At this stage clusters are given an average kinetic energy of 622 eV. They then enter the mass filter (Fig. 2(d)) where a high voltage pulse is applied to the mass filter as the species of interest enter and is stopped before the species leave the filter to facilitate the elimination of neighbouring masses. The mass selected clusters then enter the energy focusing region (Fig. 2(e)). In this region, faster clusters are ahead, and there is a linear relation (to first order) between their kinetic energy and their position along the propagation axis. By applying a pulsed high voltage in the focusing region (e), their kinetic energy dispersion is then compensated to first order. The sharp timing of the pulsed voltages ensures that only masses of interest are properly energy focused. The clusters of interest are then decelerated by an electrostatic potential barrier (Fig. 2(f)). The potential is shut down at the end of the barrier, in the zero field region. The combination of precisely timed voltage pulses applied to electrodes (d), (e) and (f) together with the potential barrier height allows to mass select a single cluster size and to control its kinetic energy in the laboratory frame. In the present experiment, the kinetic energy of the cluster in the laboratory frame was varied between 5 and 50 eV. The kinetic energy distributions have an estimated full width at half maximum of about 4 eV. The pressure in the mass selection region is about 1×10^{-6} mbar. The average number of collisions with the residual gas in this region is estimated to be less than 10^{-3}.

The clusters then fly through the collision cell (g) of length $l_{cel} = 5$ cm. In this cell a controlled amount of neon gas is introduced. The pressure is kept as low as possible to limit the effect of multiple collisions. Typical neon pressure is 10^{-4} mbar, leading to an estimated average number of collisions of around 0.1.

The center of mass (COM) collision energy is given by:

$$E_{COM} = \frac{m}{M+m}E_k + \frac{3}{2}\frac{M}{M+m}k_B T_{cel} \quad (1)$$

where T_{cel} is the collision cell temperature at 295 K, M is the cluster mass, m is the neon atom mass, and E_k is the laboratory frame kinetic energy. The distribution of collision energies is the result of the convolution of the thermal distribution of neon atom kinetic energies with the distribution of laboratory frame kinetic energies. For $(H_2O)_{21}H^+$ clusters, the range of center-of-mass collision energies E_{COM} investigated goes from 0.29 to 2.54 eV. The width of the E_{COM} distributions originates essentially from the thermal distribution of the neon atoms at 300 K. The full width at half maximum evolves from about 300 meV at E_{COM}=0.29 eV to 800 meV at E_{COM}=2.54 eV (see the Supplementary Materials for plots of the E_{COM} distributions.)

After their flight trough the collision cell, the clusters fly freely for a short distance until they reach the second Wiley-McLaren acceleration stage (h). At this stage, pulsed high voltages are applied so that they are accelerated towards a reflectron (i) and finally directed towards a pair of microchannel plates (j) where they are detected.

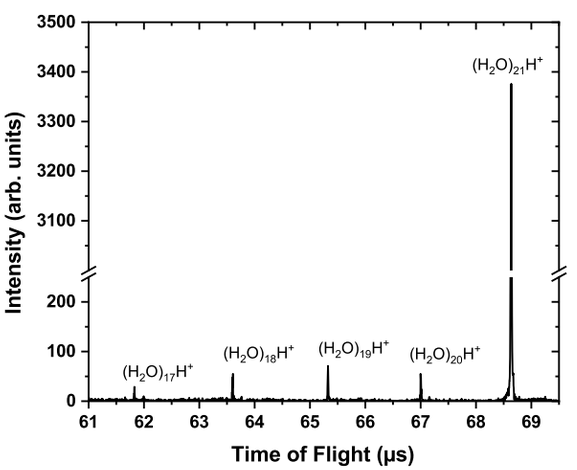

FIG. 3. TOF-MS resulting from the collision of mass-selected $(H_2O)_{21}H^+$ with neon at 2.54 eV center-of-mass collision energy. Note the break in the vertical scale.

Our experimental observable consists of time-of-flight mass spectra (TOF-MS) recorded as a function of cluster collision energy. For each collision energy, two TOF-MS are recorded, with and without gas in the collision cell. The TOF-MS without gas in the collision cell is

used to subtract the background signal. An example of the resulting TOF-MS is shown in Figure 3 (see the Supplementary Materials for the background subtraction). In this example, $(H_2O)_{21}H^+$ clusters were mass-selected at 50 eV, which results in a collision energy of 2.54 eV. The main peak at 68.64 µs corresponds to the intact parent while smaller peaks at shorter times are due to sequential losses of neutral water molecules. Here we observe up to four losses of water molecules from the parent peak.

From these TOF-MS we deduce the total fragmentation cross section as:

$$\sigma_{frag} = \frac{-\ln(I/I_0)}{\rho l_{cel}} \tag{2}$$

where ρ is the density of neon atoms in the collision cell, I is the intensity of the parent ion signal, l_{cel} is the collision cell length and I_0 is the sum of the parent ion plus all fragments signals.

The partial fragmentation cross sections σ_i for the loss of i water molecules are given by:

$$\sigma_i = \frac{I_i}{\sum_i I_i}\sigma_{frag} \tag{3}$$

where I_i is the intensity of the peak corresponding to the loss of i neutral water molecules.

For each parent cluster sizes, the experiments were repeated five times on different days and for slightly different collision cell pressure values.

III. THEORETICAL METHODS

A. Computational Methods

The initial configurations used to perform quantum chemical calculations were previously published low-energy structures of each cluster $(H_2O)_nH^+$ (n=15-23). For n=20-23, the configurations we considered are the lowest-energy structures previously obtained by Korchagina *et al.* through an extensive exploration of the potential energy surface of these species at the SCC-DFTB level in combination with parallel-tempering molecular dynamics (PTMD).[26] In this study, the starting structures for $(H_2O)_{20}H^+$ and $(H_2O)_{21}H^+$ were the ones published by Hodges and Wales and obtained using force fields and the Basin Hopping algorithm.[19] For $(H_2O)_{22}H^+$ and $(H_2O)_{23}H^+$, the initial structures were constructed by hand. For n=15-19, we directly considered the structures published by Hodges and Wales[19] as initial configuration. Further geometry optimisations were performed at the MP2, DFT and SCC-DFTB

levels of theory. DFT and MP2 calculations were performed with the Gaussian 09 package,[39] an all-electron Def2TZVP basis-set,[40,41] a tight criterion for geometry convergence and an ultrafine grid for the numerical integration. The PBE0 hybrid functional was used with and without empirical corrections.[42] In the latter case, the DFT-D3 dispersion correction from Grimme *et al.* was used.[43] Dissociation energies were calculated as differences in energy as: $D_n = E_n - E_{n+1} - E_n^{ZPE} + E_{n+1}^{ZPE}$.

Vibrational frequencies were further evaluated from the optimised structures considering the harmonic approximation. No complex frequency was detected. Overall, whatever the level of theory considered, the vibrational frequency density of states are rather similar. Consequently, in the PST approach, we considered only the SCC-DFTB frequencies. Zero point energies (ZPE) were deduced from the harmonic vibrational frequencies and taken into account in D_n (see above) at the PBE0, PBE0-D3 and SCC-DFTB levels of theory. ZPE corrections to the dissociation energies are plotted in Figure 4. Very similar behaviours are observed for PBE0 and PBE0-D3 calculations. SCC-DFTB shows different results, but the values for the ZPE correction term to D_n, i.e. $-E_n^{ZPE} + E_{n+1}^{ZPE}$, is of a similar small order of magnitude whatever the theoretical level considered. Therefore, in order to include ZPE corrections for MP2 calculations, for which direct calculation was too costly, we considered the ZPE corrections obtained at the PBE0-D3 level of theory.

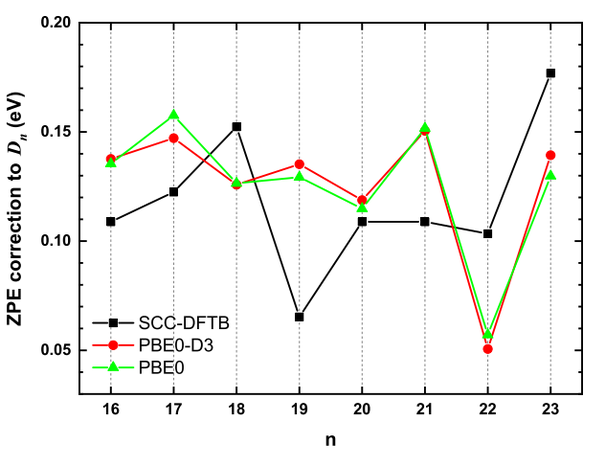

FIG. 4. Zero-point energy corrections to the dissociation energies of protonated water clusters as a function of the cluster size at different levels of theory. Black: SCC-DFTB. Red: PBE0-D3. Green triangles: PBE0.

B. PST dissociation rate

In order to extract dissociation energies from experimental TCID results, dissociation rates are required. We have used Phase Space Theory[44–46] to calculate dissociation rates. Although the absolute value of the dissociation rate may be questionable, using PST has several advantages. Firstly, PST assumes that the transition state is defined at the maximum of the centrifugal barrier (loose transition state). Consequently, the densities of states and the total number of states need only be known for the lower-energy geometries of the parent and fragments. It is therefore not necessary to search for the precise location of the transition state, a task generally difficult for highly flexible systems such as water clusters.

Secondly, the use of PST not only enables us to calculate the dissociation rate, but also to obtain the energy partitioning between internal energies of the fragments, relative kinetic energy and rotational energies. This is particularly important for studying the fragmentation of large clusters, for which a dissociation cascade occurs after collision. PST is generally recognized as being better able to give the distribution of energy between fragments than the absolute dissociation rate.[47] Calvo *et al.* have shown, for example, that PST is capable of predicting the distributions of kinetic energy release and relative rotation number J_r[48].

Thirdly, PST takes into account conservation of both energy and total angular momentum.

The long range interaction between the charged fragment cluster and the evaporated neutral molecule is considered to be dominated by the ion-polar interaction. For the present study, we consider that the effective long-range potential between the charged cluster and the neutral water molecule is therefore given by:

$$V_{eff} = -\frac{C_4}{r^4} + \frac{L^2\hbar^2}{2\mu r} \tag{4}$$

where r is the distance between the products and μ the reduced mass. The coefficient C_4 is given as $C_4 = \frac{1}{2}\alpha\frac{e^2}{4\pi\varepsilon_0}$, where $\alpha = 1.47$ Å^3 is the water molecule polarisability. Angular momentum and energy conservation together with the constraint of overcoming the centrifugal barrier leads to a minimal required rotational-translational energy $\varepsilon_{tr}^{\ddagger}$:[44–46,49]

$$\varepsilon_{tr}^{\ddagger} = \left(\frac{L^{\dagger}}{b_4}\right)^4 + B_r(L^{\dagger} - J)^2, \tag{5}$$

where $B_r = \frac{B_1 B_2}{B_1 + B_2}$, B_1 and B_2 being the rotational constants of the products. The constant

b_4 depends only on the potential and the fragment masses:

$$b_4 = \frac{2}{\hbar}\sqrt{\mu}(C_4)^{1/4}, \tag{6}$$

The angular momentum $L^\dagger$ corresponding to the minimal energy $\varepsilon_{tr}^{\ddagger}$ is:

$$L^\dagger = \left(\frac{1}{2}B_r b_4^4\right)^{1/3}\left((S+J/2)^{1/3} - (S-J/2)^{1/3}\right), \tag{7}$$

with

$$S = \sqrt{\frac{J^2}{4} + \frac{B_r b_4^4}{54}}, \tag{8}$$

The expression for the PST differential dissociation rate is[44–46,49]:

$$R_{evap}(E_v, E_r, E_{rel}, J) = A\frac{N_1(E_v)N_2(E_f - E_v - E_{rel} - E_r)N_x(E_r, E_{rel}, J)}{h(2J+1)N(E,J)} \tag{9}$$

where N_1 and N_2 are the harmonic vibrational densities of states of the fragments, N_x is the density of external states of the fragments and A an arbitrary prefactor. This prefactor is introduced to allow scaling of the total dissociation rate. Indeed, due to the different approximations employed, there are uncertainties on the absolute value of the dissociation rate. As will be shown in section IV C, this prefactor A can be used to probe the sensitivity of our dissociation energies determination against the absolute value of the dissociation rates. E_f is the total energy available in the parent for fragmentation $E_f = E + E_{rot} - D$, with the rotational energy of the parent $E_{rot} = B_0 J(J+1)$. In the case of spherical symmetry for the fragments, the expression for N_x reduces to five cases which depend on the relative values of J, $J_r^* = \sqrt{E_r/B_r}$ and $L^* = b_4 E_t^{1/4}$[44,49] and are given in the Supplementary Materials.

Among the approximations used, only harmonic vibrations are considered and the parents and the products are both considered to have spherical symmetries.

Harmonic frequencies are obtained from theoretical calculations at the SCC-DFTB level of theory. They compare well with harmonic frequencies obtained from higher-level calculations on small water clusters (n=3 to 6).[50] As is commonly done,[51,52] a global scaling factor of 0.95 was applied to the frequencies in order to take into account to some extent the anharmonicity of these systems. This allows obtaining a good agreement with the experimental vibrational frequencies of the gas phase water molecule, protonated dimer[53], bulk ice[54] and liquid water[55] (see the Supplementary Materials). For the sake of completeness, simulations considering

frequencies calculated at the PBE0-D3 were also performed. The corresponding dissociation energies are provided in the supplementary material and hardly differ from the ones presented below. This demonstrates that the present methodology is only weakly sensitive to small deviations in the considered frequencies.

The total dissociation rate is in principle obtained by integration of Eq. 9 over the vibrational energy E_v, the relative rotational energy E_r and the relative translational energy E_{rel} under the constraints of total angular momentum and energy conservation given by:

$$\begin{aligned} E_r + E_{rel} &\geq y_m \\ E_v + E_{rel} + E_r &\leq E_f \\ J_r^* &\geq J - L^* \text{ if } L^* < J \\ L^* &\geq J - J_r^* \text{ if } J_r^* < J \end{aligned} \tag{10}$$

The expression for k_{diss} is:

$$k_{diss}(E,J) = A\frac{\int dE_v \int dE_{rel} \int dE_r N_1(E_v) N_2(E_f - E_v - E_{rel} - E_r) N_x(E_r, E_{rel}, J)}{h(2J+1)N(E,J)} \tag{11}$$

which can be reformulated as:

$$k_{diss}(E,J) = A\frac{G(E_f,J)}{h(2J+1)N(E,J)} \tag{12}$$

where $G(E_f, J)$ is the total number of states of the fragments at the total energy E_f. Forst gave a route to obtain directly the total number of states $G(E_f, J)$ under the constraint of energy and total angular momentum conservation[49,56,57] and without the need to perform the triple integration in Eq.11.

Finally, the probability $P(E_v, E_{rel}, E_r, J)$ of having fragments with relative translational and rotational energies E_{rel} and E_r and internal energy E_v in the charged fragment is:

$$P(E_v, E_r, E_{rel}, J) = \frac{N_1(E_v) N_2(E_f - E_v - E_{rel} - E_r) N_x(E_r, E_{rel}, J)}{G(E_f, J)} dE_v dE_r dE_{rel} \tag{13}$$

The above expressions for the total dissociation rate and the probability distribution of energies among fragments will be used in section IV.

IV. THRESHOLD COLLISION INDUCED DISSOCIATION

A. Experimental results

The experimental results are presented in Figures 5-7 for cluster sizes of n=19 to 23. In theses figures, the total TCID cross section is plotted as a function of the COM collision energy, along with the partial cross-sections corresponding to the loss of 1 to 4 water molecules.

For all sizes a common behaviour can be observed. The total cross section begins to increase after a COM collision energy threshold and then somewhat plateaus. For the partial cross sections, successive thresholds are observed for the appearance of daughter ions of decreasing sizes (or equivalently for the loss of an increased number of neutral water molecules). From these curves we can already see that the initial loss threshold of a single water molecule is size dependent. In particular, we note that for n=21 the threshold seems somewhat higher than for the other sizes, whereas for n=22 it seems lower. This is further confirmed by fitting the total cross-sections with a Sigmoid function. The deduced threshold from such fits shows an increase by 10% for n=21 and a decrease by 12% for n=22, with respect to the average (see Supplementary Materials). However, this trend needs to be confirmed by further analysis in order to be more quantitative. This is done in the next section.

For all sizes, the magnitude of the total fragmentation cross section at high collision energy is quite similar, with values in the range of 40 to 50 Å^2. This is not surprising since one would not expect a huge variation in geometrical cross section in such a small size range. Again, this is discussed in more detail later.

B. Modeling

In order to model the TCID cross sections several processes must be taken into account, such as the collision rate, the collision energy transfer and the statistical dissociation rate.

First, the probability of a collision occurring must be calculated. This is given by:

$$P_C = 1 - e^{-k_c t} \tag{14}$$

where k_c is the collision rate and t the time. k_c depends on the experimental conditions and

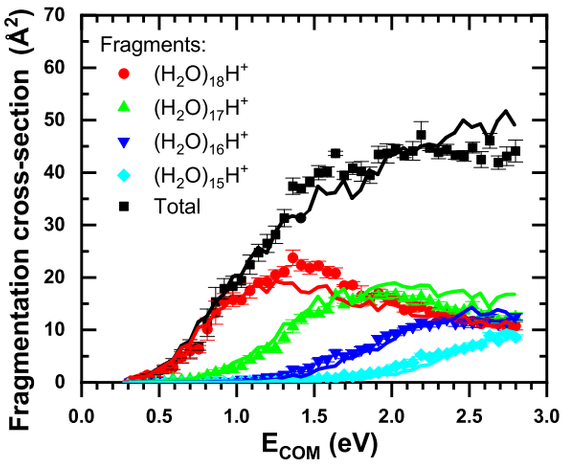

FIG. 5. TCID cross section for mass-selected $(H_2O)_{19}H^+$ colliding with neon as a function of the COM collision energy. The total cross section is plotted as black squares. Partials cross sections corresponding to the loss of 1 up to 4 water molecules are plotted as coloured symbols (1: red circles, 2: green up triangles, 3: blue down triangle, 4: cyan diamonds). Standard errors are plotted as error bars. The lines correspond to the fit to the data using the model described in section IV D.

especially on the cluster kinetic energy. The collision rate expression is:

$$k_c = \rho \sigma_{geo} v_{rel} \tag{15}$$

where ρ is the density of atoms in the cell, σ_{geo} is the geometrical cross section and v_{rel} is the relative velocity between the atom and the cluster.

Part of the collision energy is expected to be transferred into internal energy of the cluster. We follow here the Line of Centers model[58] and assume that the transferred energy is given by:

$$E_t = \left(1 - \left(\frac{b}{R+r}\right)^2\right) E_{COM} \tag{16}$$

where b is the impact parameter, R is the cluster radius and r is the impinging atom radius. The distribution of impact parameters is given by $f_b(b)db = \frac{2b}{(R+r)^2}db$ with $b_{max} = (R+r)$.

Upon impact, if enough energy is deposited in the cluster, it can dissociate. Dissociation is assumed to occur statistically. In this study, we use the PST to calculate the statistical

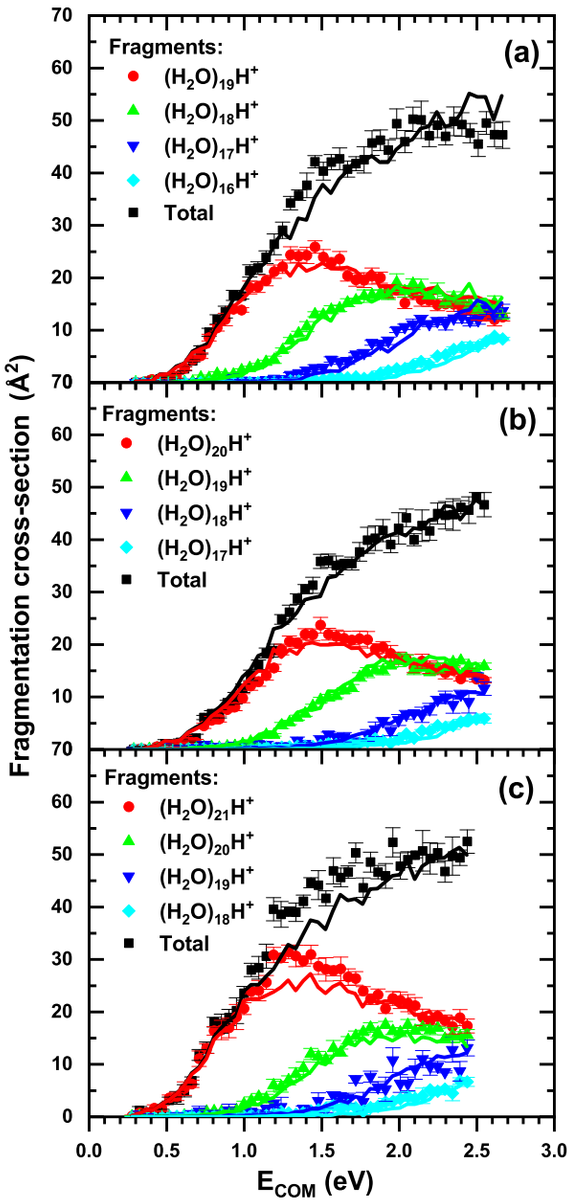

FIG. 6. TCID cross section for mass-selected (a) $(H_2O)_{20}H^+$, (b) $(H_2O)_{21}H^+$ and (c) $(H_2O)_{22}H^+$ colliding with neon as a function of the COM collision energy. The total cross section is plotted as black squares. Partials cross sections corresponding to the loss of 1 up to 4 water molecules are plotted as coloured symbols (1: red circles, 2: green up triangles, 3: blue down triangle, 4: cyan diamonds). Standard errors are plotted as error bars. The lines correspond to the fit to the data using the model described in section IV D.

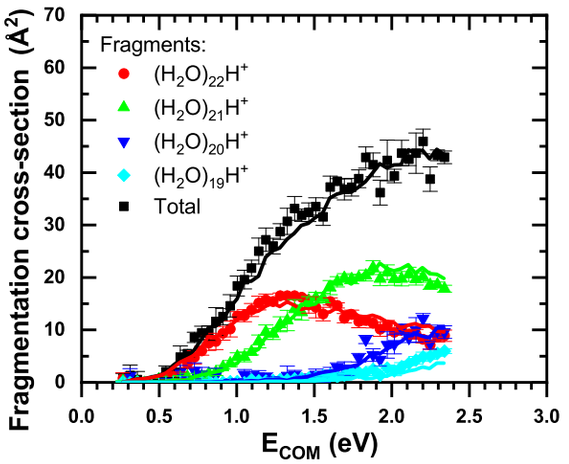

FIG. 7. TCID cross section for mass-selected $(H_2O)_{23}H^+$ colliding with neon as a function of the COM collision energy. The total cross section is plotted as black squares. Partials cross sections corresponding to the loss of 1 up to 4 water molecules are plotted as coloured symbols (1: red circles, 2: green up triangles, 3: blue down triangle, 4: cyan diamonds). Standard errors are plotted as error bars. The lines correspond to the fit to the data using the model described in section IV D.

dissociation rate k_{diss}. The dissociation probability is given by:

$$P_D = 1 - e^{-k_{diss}t} \tag{17}$$

The dissociation rate depends on the internal energy of the cluster, its rotational energy and on the dissociation energy, $k_{diss} = k_{diss}(E, E_0, J)$. The internal energy of the cluster after collision is given by:

$$E = E_{ini} + E_t \tag{18}$$

where E_{ini} is the initial thermal energy of the cluster at 25 K. The initial energy is :

$$E_{ini} = \sum_i n_i \hbar\omega_i \tag{19}$$

where n_i is the occupation number of the vibrational mode i at frequency ω_i. The probability to have n_i quanta in mode i is given by:

$$P(n_i) = (1 - e^{-\hbar\omega_i/k_BT})e^{-n_i\hbar\omega_i/k_BT} \tag{20}$$

The distribution of initial internal vibrational energy at temperature T, $P_T(E_{ini})$, is obtained by populating the vibrational modes according to Eq. 20. The probability to have a parent cluster with a rotational quantum number J is taken as:

$$P_J(J) = \frac{4}{\sqrt{\pi}} \left(\frac{B_0}{k_B T} \right)^{3/2} J^2 e^{-J^2 B_0 / k_B T} \tag{21}$$

Following the above formalism, the experimental signal is modelled by simulating the ion trajectories. We use a Monte Carlo integration scheme to sample the different parameters involved, such as the initial internal energies of the clusters, the initial rotational numbers, and the velocities of the rare gas atoms. Collisions and dissociation events can occur at every time step according to their probabilities. The collision probability is given by P_C (Eq. 14) and the dissociation probability P_D by Eq. 17. For each collision, the impact parameter is selected according to the $f_b(b)$ distribution. Following a collision or dissociation event, the ion velocities are updated so that possible ion losses are taken into account. The internal energies of he fragments, the rotational numbers and relative kinetic energies are obtained by using the probability given by Eq.13.

This modelling reproduces the experimental TOF-MS well. It makes it possible to take into account the successive dissociations so that the complete fragmentation pattern can be reproduced. However, such a modelling is quite time-consuming and therefore does not allow to easily perform global optimisations in order to fit the experimental data. Nevertheless, if one is primarily interested in the first dissociation threshold, a simple expression for the cross section can be used that allows easy fitting of the experimental data. The total fragmentation cross section can indeed be directly obtained by integrating on the impact parameter:

$$\sigma = \sigma_{geo} \int_0^{b_{max}} f_b(b) db P_D \tag{22}$$

This equation is similar to that given by Armentrout *et al.*[31]. By changing the integration variable from b to E_t we recover the expression given in [31]. However, we consider that the current formulation is more natural because it explicitly displays the energy transfer model used. In order to better describe the collisional energy transfer, Chen *et al.*[59,60] suggested to deduce the maximal impact parameter that leads to collision explicitly from Langevin theory[61,62]. However, in the present case, the maximal impact parameter deduced from such a Langevin theory would be smaller than the actual geometric size of the cluster.

Eventually, the cross section has to be averaged over the distribution of initial internal energies, the distribution of rotational number J as well as over the relative velocity distribution:

$$\sigma = \sigma_{geo} \sum_{J} \sum_{E_{ini}} \int_0^\infty d_{vrel} \int_0^{b_{max}} db f_v(v_{rel}) f_b(b) P_C P_D P_T(E_{ini}) P_J(J) \tag{23}$$

Since we start with cold clusters with very little internal energy, the summation over the internal energy distribution can be removed. Instead we use the average internal energy at 25 K, which is calculated as:

$$E = \sum_i \frac{\hbar\omega_i}{e^{\hbar\omega_i/kBT} - 1} \tag{24}$$

For the size n=21, we derived an internal energy of 7 meV at 25 K.

Similarly, taking $J = 0$ or the most probable value of J does not drastically change the results for the total cross section and the summation over the J-distribution is therefore also removed. Eventually, the expression for the TCID cross section resumes to:

$$\sigma = \sigma_{geo} \int_0^\infty d_{vrel} \int_0^{b_{max}} db f_v(v_{rel}) f_b(b) P_C P_D \tag{25}$$

This approximate expression gives an efficient way to evaluate the total TCID cross section so that a quick fit to the experimental data can be performed. However, it does not allow to treat sequential dissociations and does not take into account possible ion losses during propagation in the experimental setup.

In the next section, the total cross sections are analysed using this last expression. We will see that such analysis has certain limitations. These can be overcome by taking into account partial cross sections, which requires the more demanding use of ion trajectory simulations together with Monte-Carlo integration.

C. Curve fitting: Total cross section

In this section it is shown that it is not possible to deduce, to a reasonable accuracy, dissociation energies using only the total fragmentation cross section of a single cluster size. Fortunately, it will be demonstrated in the next section that a cross analysis of partial fragmentation cross sections of a parent cluster and neighbouring sizes leads to the determination of reliable dissociation energies with a good accuracy, and with a single choice of parameters consistent over the whole size range and the whole set of experimental data.

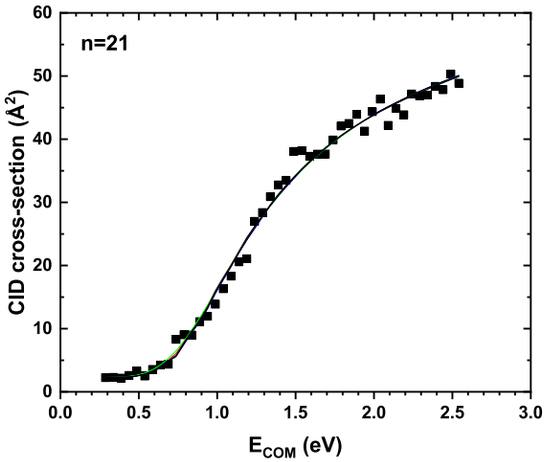

FIG. 8. Total TCID cross section for n=21 protonated water cluster. The experimental data are represented as squares. Five theoretical curves are plotted as lines, which are virtually indistinguishable. These five curves correspond to five assumed different prefactor which imply five possible dissociation energies (see text).

In Figure 8 we show the total TCID cross section for the n=21 protonated water cluster. Together with the experimental data are plotted five different theoretical curves obtained by using Eq. 25. Virtually identical fit quality can be obtained with different couples of prefactor A and dissociation energies. For instance by multiplying the dissociation rate by $10^{\pm 6}$, the deduced dissociation energies vary from about 0.3 to 0.6 eV. Table I gives the values used to plot the curves in Fig. 8. The $+\infty$ value means that we have taken $P_D = 1$ in Eq. 25.

Prefactor	10^{-6}	10^{0}	10^{6}	10^{12}	$+\infty$
n=19	0.29	0.45	0.57	0.63	0.64
n=20	0.26	0.44	0.56	0.64	0.69
n=21	0.33	0.51	0.64	0.73	0.79
n=22	0.23	0.38	0.50	0.57	0.61
n=23	0.29	0.45	0.57	0.65	0.71

TABLE I. Prefactor and dissociation energies in eV used to fit the total fragmentation cross-sections for sizes n=19-23. An example of the fit is given for n=21 in Fig.8.

We have fitted the total cross section for all sizes from n=19 to n=23, the obtained dissociation energies are given in Table I. In Figure 9 are plotted the dissociation energies relative to the value for n=21, for the five values of the prefactor.

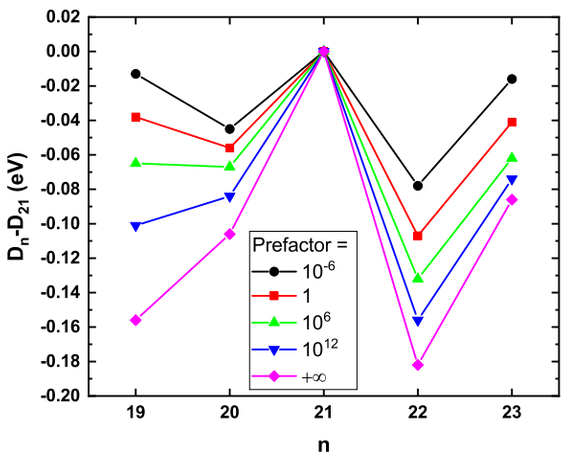

FIG. 9. Relative dissociation energies obtained from the fit of the total TCID cross section using different values of the prefactor for the dissociation rate.

Although changing the prefactor by orders of magnitude changes drastically the absolute value of the dissociation energies, the relative values remain preserved with a reasonable accuracy (the different dissociation energies relative to the one for n=21 only vary within ±0.1 eV).

Nevertheless, Figures 8 and 9 illustrate the importance of having a good estimate of the dissociation rate when extracting dissociation energies from TCID experiments, which is not easily achieved in such complex systems. The data analysis presented above is clearly insufficient to provide accurate and reliable values of dissociation energies. However, we show in the next section that if we exploit the whole data set, i.e. not only the total TCID cross-section but also the subsequent dissociation channels, it is possible to set strict limits on the prefactor value and thus extract reliable dissociation energies.

D. Curve fitting: Partial cross sections

In order to reproduce not only the total cross section but also the partial cross sections one has to take into account cascading dissociation events: after a collision, if the internal energy

of the cluster is high enough, several water molecules can dissociate sequentially from the cluster. Treating these sequential losses requires a complete simulation of ion trajectories through the entire experimental device, and treating collision and evaporation events at each time step. In addition, after each dissociation, the distribution of relative kinetic and internal energies between fragments must be taken into account. As already mentioned, global fitting of the whole data set with such a method would be very time-consuming. For this reason, we have devised a strategy for extracting dissociation energies from experimental curves requiring a reasonable number of simulations. The following sequential strategy is used, in which accuracy is improved from one step to the next:

Firstly, for a parent cluster of size n, we consider that only the first dissociation takes place and that subsequent dissociation are forbidden. From trajectory calculations, we extract a cross-section which is equivalent to the total experimental cross-section. For each dissociation energy value ranging from 0.35 to 6.5 eV in steps of 0.03 eV, we compare our simulated results with the total experimental cross-section, and retain the dissociation energy that gives the best fit. We then vary the dissociation energy D_{n-1}, this time allowing for up to two losses of water molecules. We thus obtain two partial cross-sections which can again be compared with experimental values. The first partial cross-section corresponds to the loss of a single water molecule, while the second partial cross-section is the sum of all the other channels, i.e. the losses of 2, 3 and 4 water molecules. This procedure is repeated until four water molecules have been lost. The maximum number of evaporation has been limited to 4 water molecules since, under our experimental conditions, the probability of evaporating more than 4 molecules is totally insignificant due to the very low internal energy reached following 4 successive evaporative cooling. This procedure minimizes the number of simulations needed to find the optimum values for dissociation energies. This operation is carried out independently for the five sizes studied. The values obtained for dissociation energies from independent measurements can then be compared, checked for consistency and the most appropriate prefactor selected. For example, from the size n=23, we can deduce dissociation energies not only for n=23 but also for n= 22, 21 and 20 from the dissociation cascade. In the whole procedure for fitting experimental results, the only adjustable parameters are the dissociation energies. However, given the number of approximations used in the PST formulation, it is conceivable that the total dissociation rates used in the simulation could be off by an unknown factor. To check the influence of such an

uncertainty, the above procedure was carried out for three different values of the prefactor A, namely 10^{-6}, 1 and 10^{6}. Here, we consider extreme values for the prefactor in order to test the sensitivity of our method for determining dissociation energies. All the obtained dissociation energies are plotted in Figure 10.

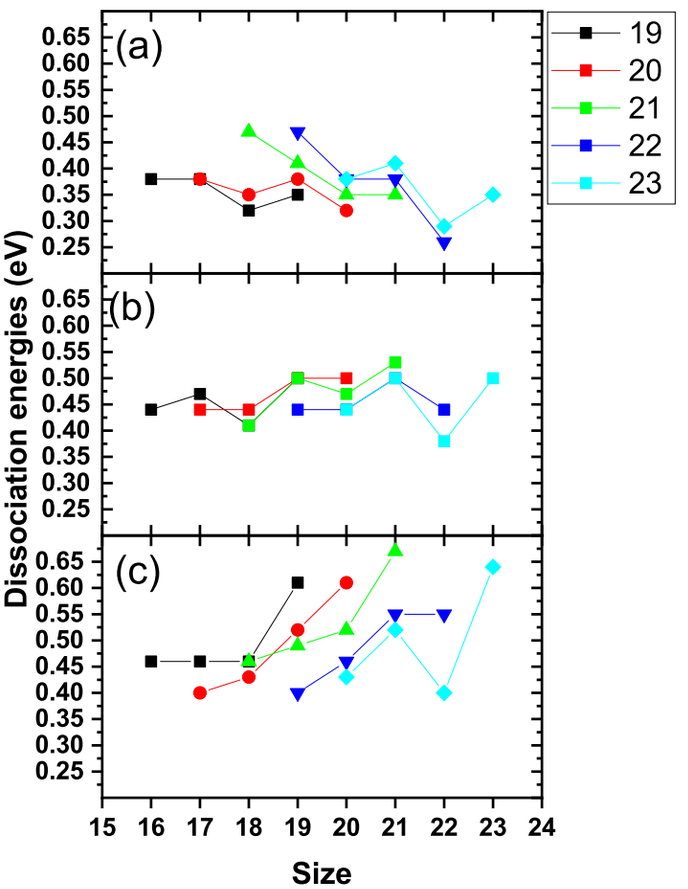

FIG. 10. Optimised dissociation energies obtained for the five cluster sizes n=19, 20, 21, 22 and 23 from the dissociation cascades. The prefactor value for the PST dissociation rate is 10^{-6} in (a), 1 in (b) and 10^{6} in (c).

In this figure, in each of the three panels (a), (b) and (c) are represented the dissociation energies obtained from the five cluster sizes n=19, 20, 21, 22, 23. For each parent size n, four dissociation energies are deduced, D_n, D_{n-1}, D_{n-2} and D_{n-3}. Ideally, we would expect all the dissociation energies deduced from different parent cluster sizes to be equal. This is not quite the case, but in panel (b), corresponding to a prefactor of 1, the dispersion of the dissociation energies obtained is the smallest.

We observe that by changing the prefactor, different absolute values of dissociation energies are obtained. Indeed, in panel (a), for a prefactor of 10^{-6}, on average the obtained dissociation energies are about 0.37 eV. In (b) (prefactor of 1) the average is about 0.46 eV, while in (c) it is about 0.50 eV. Increasing the prefactor results in higher dissociation energies, at least for the first dissociation threshold. Looking at the next threshold, the situation is less clear-cut.

For the lowest prefactor value, Figure 10(a), for a given parent size, the dissociation energies deduced from the cascade tend to increase with the number of dissociation. It is as if too much energy remains in the system during dissociation, so that to reproduce the experimental data, the dissociation energy has to be increased. As a result, the different sets of dissociation energies are poorly matched to each other. In Figure 10(c), the prefactor has been taken equal to 10^6. In this case, on the contrary, after the first dissociation, too little energy remains in the system, so subsequent dissociation energies have to be lowered to match the experimental data. Once again, this leads to relatively low consistency between the different sets of dissociation values.

The case with a prefactor of 1 shown in Figure 10(b) gives the most consistent set of dissociation energy values. The overall agreement is quite good, but there are nevertheless a few discrepancies that deserve comment. In particular, the dissociation energy deduced for n=19 from parent size n=22 is in relatively poor agreement with the other determinations from parent sizes n=19, 20 and 21. However, for parent size n=22, this corresponds to the very last event in the cascade, for which, firstly the amount of signal is quite small, and secondly, the error accumulation from the model is the biggest. We therefore do not expect a perfect agreement under these conditions. The other dissociation energy with rather different values is that of n=22. In particular, parent size n=23 gives a much lower value for D_{22} than is obtained from parent size n=22. In this case, the disagreement could be linked to real physical effects. In particular, we could imagine that dissociation of the n=23 cluster leads to a less-bonded n=22 daughter cluster than the n=22 parent cluster produced in the source.

In our treatment of the dissociation cascade, we assume that upon dissociation of size n the lowest-energy n-1 conformer is formed. This assumption could become invalid if the dissociation leads to conformers with substantially different structures. In this case, first the dissociation energy of such structures could differ from the one of the lowest lying isomers.

The relatively good consistency obtained for the different dissociation cascades indicates that such effects play a minor role here. Secondly, major structural changes might affect the vibrational frequencies and therefore change the density of states used to calculate the dissociation rate. However, for all cluster sizes studied, the size to size differences in calculated structures do not show up significantly in the vibrational modes (see Supplementary Materials for the comparison of the vibrational modes for the different sizes.)

The use of dissociation cascades therefore makes it possible to set strict limits on the prefactor and dissociation energies. Indeed, if we consider only the first dissociation threshold, as shown in the previous section, different combinations of prefactor and dissociation energy give equivalent results. However, if we consider the second dissociation, this is no longer the case. For a combination of too low a dissociation energy and too high a prefactor, too much internal energy remains in the daughter cluster, and to reproduce the experimental curves, a higher dissociation energy must be assumed. We therefore observe a tendency for dissociation energy to increase systematically with the order of dissociation. On the contrary, if we combine too high a dissociation energy with too low a prefactor, we observe the opposite, i.e. a tendency for the dissociation energy to decrease with the order of dissociation.

The best fits to the experimental data, using a prefactor of 1 and the dissociation energies given in Figure10(b), are shown as solid lines in Figures 5 to 7. From now on, we will only discuss the dissociation energies obtained with a prefactor of 1.

The dissociation energies obtained in Figure 10(b) are averaged and compared with previous studies in Figure 11. Our results are shown with a constant error bar of 0.03 eV corresponding to the steps used in the search for optimum values of the dissociation energies.

V. DISCUSSION

In the aforementioned previous studies[15,17,18,30] the protonated water clusters are produced using different techniques. For instance, Magnera *et al.* used fast ion bombardment of ice to produce the clusters. Hansen *et al.* used an electrospray source. Shi *et al.* used a supersonic expansion to form water neutral clusters with methyl iodide impurity. Multiphoton ionization is then used to electronically excite the methyl iodide molecule and form protonated water clusters. In Bruzzie *et al.* the clusters are also formed in a supersonic

expansion, but ionization is performed by 70 eV electron impact.

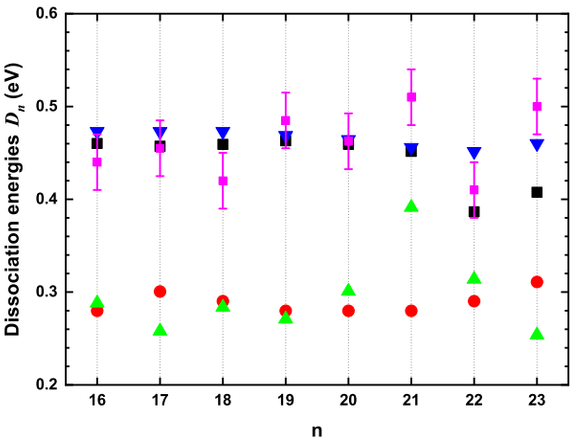

FIG. 11. Dissociation energies of protonated water clusters as a function of the cluster size from previous experimental studies compared to the present study. Black squares: K. Hansen *et al.*, Ref. 18. Red circles: Bruzzie *et al.*, Ref. 30. Green triangles: Magnera *et al.*, Ref. 15. Blue triangles: Shi *et al.*, Ref. 17. Results from the present work are plotted as magenta squares with error bars.

If we consider the absolute values of dissociation energies, our values are compatible with the work of Hansen *et al.* and Shi *et al.*, with typical values around 0.47 eV. We note that the obtained dissociation energies approach the enthalpies of vaporization of bulk ice, which evolves between 0.49 and 0.53 eV/molecule between 0 and 273 K.[63] The values are definitively not in line with the work of Magnera *et al.* and Bruzzie *et al.* In Magnera *et al.*'s work, dissociation energies are obtained from the difference between daughter ion appearance thresholds. The effect of kinetic shift is not included in the analysis. In addition, the authors point out that the parent ions are probably quite hot[15,64], with the first dissociation occurring at very low collision energy. Consequently, the reliability of this study is questionable with regard to absolute values of dissociation energies, particularly for such large sizes for which kinetic displacements are important. We note that in our analysis using a prefactor A=10^{-6} we obtain dissociation energies that are compatible with those deduced by Magnera *et al.* and Bruzzie *et al.* However, using such a value for the prefactor does not fully reproduce the complete dissociation cascade of the present study. Furthermore, while it is certainly difficult to obtain a reliable absolute dissociation rate using PST[47,48], we would not expect

the dissociation rate to be off by such an extent.

In the work of Bruzzie *et al.*, the dissociation energies are deduced from the kinetic energy release of the fragmented ions. The fragmentation follows from the 70 eV electron impact ionization of neutral water clusters. In this study, the parent ions are therefore probably relatively hot, with a lot of isomers populated. Their deduced dissociation energies are found to be compatible with the breaking of a single hydrogen bond and the authors conclude that for protonated water clusters larger than n=6, the clusters decay by breaking a single hydrogen bond. Their method might be only sensitive to the transition state where the water molecule about to leave the cluster might indeed make a single H-bond with the cluster. However in our experiment, we start with a low internal energy in the clusters. For such low-energy isomers all water molecules make multiple H-bond within the cluster. The internal energy brought by collisions therefore involve the breaking of several H-bonds. In this respect, current results probably probe ground-state structures more realistically.

Around size n=21, other important differences exist compared to previous studies. In Shi *et al.* and Bruzzie *et al.*, the authors observed a very weak dependence of dissociation energy on size. In Hansen *et al.* the authors observe that dissociation energies drop at n=22 after a high binding energy plateau. Our results show that the dissociation energy of size n=22 is significantly lower than that of clusters of similar size, while that of size n=21 is on the contrary slightly higher. We note that in the three previous studies the determination of the binding energies is based on the spontaneous decay of hot parent clusters. In Magnera *et al.*, where the authors used CID, there is a clear bump at n=21 in the determined binding energies. However, as already mentioned, this study lacks the inclusion of kinetic shifts in the analysis.

The anti-magic character of the n=22 size is manifested in our measurements by a lower binding energy than neighbouring sizes. Two possible structures for the n=22 protonated water cluster have been proposed.[6,22] One is a a distorted cage. The other structure features a dangling water molecule attached to the n=21 protonated water cluster. For the distorted cage structure, dissociation involves the breaking of at least two hydrogen bonds. From the latter structure, we would expect a much lower dissociation energy than that observed in our study since it involves the breaking of a single hydrogen bond. On the other hand, the magic character of size n=21 is reflected in our measurements by a binding energy higher than that of neighbouring sizes n=20,22 and slightly higher than of sizes n=19,23.

The above observations indicate that our experiment enables us to study CID fragmentation of low-energy isomers. As the clusters are thermalized at low temperatures, their populations are expected to be limited to low-energy isomers and to have very low internal energy prior to collision. In addition, the use of CID has the advantage that the amount of internal energy brought by the collision is rather well controlled. For methods based on spontaneous evaporation analysis, the structures considered result from the evaporation cascade of a population of hot isomers. These latter methods may also be biased due to their sensitivity to the transition state. Therefore, the combination of CID and a low-temperature thermalized cluster source is certainly advantageous if we want to extract binding energies that can be directly compared with theoretical calculations.

The theoretical results regarding D_n are summarized in Figure 12. Calculations at the MP2 level by Singh *et al.* give similar values for the dissociation energies of $(H_2O)_{21}H^+$ and $(H_2O)_{22}H^+$ (Singh *et al* only considered these two sizes.).[22] Overall, whatever the level of theory, $(H_2O)_{21}H^+$ displays an enhanced D_n value, *i.e.* an enhanced stability, with respect to neighbouring sizes. A comparison of experimental and theoretical values of D_n is provided in the same figure. Satisfactory qualitative agreement is obtained with regard to the magnitude of dissociation energies. Moreover, the experimental values are very close to the SCC-DFTB D_n values, with differences of less than 0.05 eV for $(H_2O)_{16-19,21}H^+$. This may be understandable considering that the SCC-DFTB potential considered here has been specifically tuned to describe binding energies in water clusters and has demonstrated good performance in modelling the phase transition in $(H_2O)_nH^+$ (n=20-23) clusters.[26] Overall, the theoretical values show larger between-size variations than the experimental values, particularly at the PBE0 level. It is worth mentioning that the calculations are performed at 0 K on a unique configuration considered to be the lowest-energy isomer while experiment probably take into account a distribution of low-energy isomers, which could explain the dependencies we observe.

VI. CONCLUSION

We have re-examined the evolution of binding energies of protonated water clusters as a function of size around the magic size n=21. Our experimental method combines a low-temperature thermalized cluster source and CID fragmentation. The reliability of our results

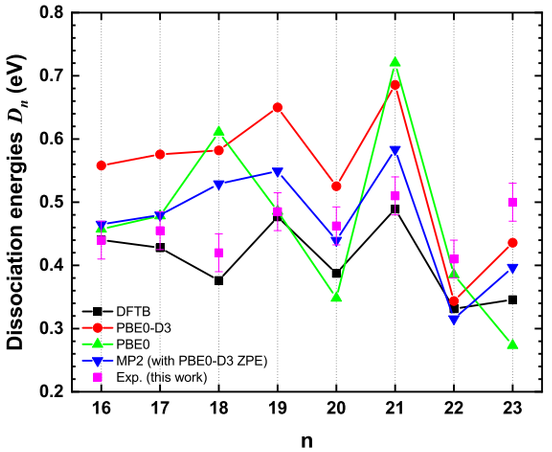

FIG. 12. Theoretical and experimental dissociation energies obtained in this work, as a function of the cluster size. Black squares: SCC-DFTB. Red circles: DFT PBE0-D3. Green triangles: DFT PBE0. Blue triangles: MP2. Magenta squares with error bars: Experimental values.

for each cluster size is strongly improved by the necessary interplay, because of dissociation cascade, between experiments conducted on neighboring sizes: This induces strong experimental constraints on the fitting parameters, and then on final result. As far as absolute values are concerned, we found good agreement with previous studies, in particular with the work of Hansen *et al.* and Shi *et al* . On the basis of the binding energies derived, we were able to confirm the magic and anti-magic characters of n=21 and 22, respectively. This result was not convincingly established in previous experiments. Our experimental results are supported by theoretical calculations for the lowest-energy structures. The calculations show more pronounced differences between sizes than the experiment, suggesting that more than one isomer is involved in the experiment despite the low thermalization temperature.

SUPPLEMENTARY MATERIALS

See the Supplementary Materials for expression of the external density of states N_x. We also provide in the Supplementary Materials break-down curves for all cluster sizes, relative kinetic energy distributions, sigmoidal fits of the fragmentation cross-sections and a comparison of the vibrational frequencies. A comparison of the dissociation energies obtained using the frequencies from the SCC-DFTB and PBE0-D3 calculations is also provided.

ACKNOWLEDGMENTS

This work received support from the European Research Council under the European Union's Seventh Framework Programme ERC-2013-SyG, Grant Agreement no. 610256, NANOCOSMOS and from CNRS through the 80—Prime program (Project Nanoeau). The authors acknowledge the supercomputing facility of CALMIP for generous allocation of computer resources (project P1320).

DATA AVAILABILITY

The data that supports the findings of this study are available within the article and the Supplementary Materials.

REFERENCES

[1]V. E. Bondybey and M. K. Beyer, International Reviews in Physical Chemistry **21**, 277 (2002).

[2]G. Hauck and F. Arnold, Nature **311**, 547 (1984), number: 5986 Publisher: Nature Publishing Group.

[3]M. Miyazaki, A. Fujii, T. Ebata, and N. Mikami, Science **304**, 1134 (2004).

[4]J.-W. Shin, N. I. Hammer, E. G. Diken, M. A. Johnson, R. S. Walters, T. D. Jaeger, M. A. Duncan, R. A. Christie, and K. D. Jordan, Science **304**, 1137 (2004).

[5]K. Mizuse, N. Mikami, and A. Fujii, Angewandte Chemie International Edition **49**, 10119 (2010).

[6]K. Mizuse and A. Fujii, Chemical Physics **419**, 2 (2013).

[7]K. A. Servage, J. A. Silveira, K. L. Fort, and D. H. Russell, The Journal of Physical Chemistry Letters **5**, 1825 (2014).

[8]S.-S. Lin, Review of Scientific Instruments **44**, 516 (1973).

[9]J. Q. Searcy and J. B. Fenn, The Journal of Chemical Physics **61**, 5282 (1974).

[10]H. R. Carlon and C. S. Harden, Applied Optics **19**, 1776 (1980).

[11]O. Echt, D. Kreisle, M. Knapp, and E. Recknagel, Chemical Physics Letters **108**, 401 (1984).

[12]H. Shinohara, U. Nagashima, and N. Nishi, Chemical Physics Letters **111**, 511 (1984).

[13]U. Nagashima, H. Shinohara, N. Nishi, and H. Tanaka, The Journal of Chemical Physics **84**, 209 (1986).

[14]X. Yang and A. W. Castleman, Journal of the American Chemical Society **111**, 6845 (1989).

[15]T. F. Magnera, D. E. David, and J. Michl, Chemical Physics Letters **182**, 363 (1991).

[16]S. Wei, W. B. Tzeng, R. G. Keesee, and A. W. Castleman, Journal of the American Chemical Society **113**, 1960 (1991).

[17]Z. Shi, J. V. Ford, S. Wei, and A. W. Castleman, The Journal of Chemical Physics **99**, 8009 (1993).

[18]K. Hansen, P. U. Andersson, and E. Uggerud, The Journal of Chemical Physics **131**, 124303 (2009).

[19]M. P. Hodges and D. J. Wales, Chemical Physics Letters **324**, 279 (2000).

[20]C.-C. Wu, C.-K. Lin, H.-C. Chang, J.-C. Jiang, J.-L. Kuo, and M. L. Klein, The Journal of Chemical Physics **122**, 074315 (2005).

[21]S. S. Iyengar, M. K. Petersen, T. J. F. Day, C. J. Burnham, V. E. Teige, and G. A. Voth, The Journal of Chemical Physics **123**, 084309 (2005).

[22]N. J. Singh, M. Park, S. K. Min, S. B. Suh, and K. S. Kim, Angewandte Chemie **118**, 3879 (2006).

[23]J. Liu, J. Yang, X. C. Zeng, S. S. Xantheas, K. Yagi, and X. He, Nature Communications **12**, 6141 (2021).

[24]T. S. Zwier, Science **304**, 1119 (2004).

[25]N. J. Singh, M. Park, S. K. Min, S. B. Suh, and K. S. Kim, Angew. Chem. Int. Ed. **45**, 3795 (2006).

[26]K. Korchagina, A. Simon, M. Rapacioli, F. Spiegelman, J.-M. L'Hermite, I. Braud, S. Zamith, and J. Cuny, Phys. Chem. Chem. Phys. **19**, 27288 (2017).

[27]J. Boulon, I. Braud, S. Zamith, P. Labastie, and J.-M. L'Hermite, The Journal of Chemical Physics **140**, 164305 (2014).

[28]N. Yang, S. C. Edington, T. H. Choi, E. V. Henderson, J. P. Heindel, S. S. Xantheas, K. D. Jordan, and M. A. Johnson, Proceedings of the National Academy of Sciences **117**, 26047 (2020), publisher: Proceedings of the National Academy of Sciences.

[29]G. Niedner-Schatteburg and V. E. Bondybey, Chemical Reviews **100**, 4059 (2000), publisher: American Chemical Society.

[30]E. Bruzzi, R. Parajuli, and A. J. Stace, International Journal of Mass Spectrometry **333**, 1 (2013).

[31]P. B. Armentrout, K. M. Ervin, and M. T. Rodgers, J. Phys. Chem. A **112**, 10071 (2008).

[32]P. B. Armentrout, Journal of the American Society for Mass Spectrometry **13**, 419 (2002).

[33]M. Elstner, D. Porezag, G. Jungnickel, J. Elsner, M. Haugk, T. Frauenheim, S. Suhai, and G. Seifert, Physical Review B **58**, 7260 (1998).

[34]P. Koskinen and V. Mäkinen, Computational Materials Science **47**, 237 (2009).

[35]T. Frauenheim, G. Seifert, M. Elsterner, Z. Hajnal, G. Jungnickel, D. Porezag, S. Suhai, and R. Scholz, physica status solidi (b) **217**, 41 (2000).

[36]F. Chirot, S. Zamith, P. Labastie, and J.-M. L'Hermite, Rev. Sci. Instrum. **77**, 063108 (2006).

[37]I. Braud, S. Zamith, and J.-M. L'Hermite, Rev. Sci. Instrum. **88**, 043102 (2017).

[38]S. Zamith, M.-C. Ji, J.-M. L'Hermite, C. Joblin, L. Dontot, M. Rapacioli, and F. Spiegelman, J. Chem. Phys. **151**, 194303 (2019).

[39]M. J. Frisch, G. W. Trucks, H. B. Schlegel, G. E. Scuseria, M. A. Robb, J. R. Cheeseman, G. Scalmani, V. Barone, B. Mennucci, G. A. Petersson, H. Nakatsuji, M. Caricato, X. Li, H. P. Hratchian, A. F. Izmaylov, J. Bloino, G. Zheng, J. L. Sonnenberg, M. Hada, M. Ehara, K. Toyota, R. Fukuda, J. Hasegawa, M. Ishida, T. Nakajima, Y. Honda, O. Kitao, H. Nakai, T. Vreven, J. A. Montgomery, Jr., J. E. Peralta, F. Ogliaro, M. Bearpark, J. J. Heyd, E. Brothers, K. N. Kudin, V. N. Staroverov, R. Kobayashi, J. Normand, K. Raghavachari, A. Rendell, J. C. Burant, S. S. Iyengar, J. Tomasi, M. Cossi, N. Rega, J. M. Millam, M. Klene, J. E. Knox, J. B. Cross, V. Bakken, C. Adamo, J. Jaramillo, R. Gomperts, R. E. Stratmann, O. Yazyev, A. J. Austin, R. Cammi, C. Pomelli, J. W. Ochterski, R. L. Martin, K. Morokuma, V. G. Zakrzewski, G. A. Voth, P. Salvador, J. J. Dannenberg, S. Dapprich, A. D. Daniels, O. Farkas, J. B. Foresman, J. V. Ortiz, J. Cioslowski, and D. J. Fox, "Gaussian–09 Revision D.01," Gaussian Inc. Wallingford CT 2009.

[40]F. Weigend and R. Ahlrichs, Phys. Chem. Chem. Phys. **7**, 3297 (2005).

[41]F. Weigend, Phys. Chem. Chem. Phys. **8**, 1057 (2006).

[42]C. Adamo and V. Barone, J. Chem. Phys. **110**, 6158 (1999).

[43]S. Grimme, J. Antony, S. Ehrlich, and H. Krieg, J. Chem. Phys. **132** (2010), 10.1063/1.3382344, 154104.

[44]W. J. Chesnavich and M. T. Bowers, Journal of the American Chemical Society **98**, 8301 (1976).

[45]W. J. Chesnavich and M. T. Bowers, The Journal of Chemical Physics **66**, 2306 (1977).

[46]W. J. Chesnavich and M. T. Bowers, Journal of the American Chemical Society **99**, 1705 (1977).

[47]S. Weerasinghe and F. G. Amar, The Journal of Chemical Physics **98**, 4967 (1993).

[48]F. Calvo, J. Douady, and F. Spiegelman, The Journal of Chemical Physics **132**, 024305 (2010).

[49]W. Forst, Unimolecular Reactions: A Concise Introduction (Cambridge University Press, 2003).

[50]J. C. Howard and G. S. Tschumper, Journal of Chemical Theory and Computation **11**, 2126 (2015).

[51]A. P. Scott and L. Radom, The Journal of Physical Chemistry **100**, 16502 (1996), publisher: American Chemical Society.

[52]M. K. Kesharwani, B. Brauer, and J. M. L. Martin, The Journal of Physical Chemistry A **119**, 1701 (2015), publisher: American Chemical Society.

[53]R. Kalescky, W. Zou, E. Kraka, and D. Cremer, Chemical Physics Letters **554**, 243 (2012).

[54]J. R. Scherer and R. G. Snyder, The Journal of Chemical Physics **67**, 4794 (2008).

[55]G. E. Walrafen and E. Pugh, Journal of Solution Chemistry **33**, 81 (2004).

[56]W. Forst, Chemical Physics Letters , 539 (1996).

[57]W. Forst, Physical Chemistry Chemical Physics , 1283 (1999).

[58]D. Levine and R. B. Bernstein, Molecular Reaction Dynamics and Chemical Reactivity (Oxford University Press, 1987).

[59]S. Narancic, A. Bach, and P. Chen, The Journal of Physical Chemistry A **111**, 7006 (2007), publisher: American Chemical Society.

[60]E. Paenurk and P. Chen, The Journal of Physical Chemistry A **125**, 1927 (2021).

[61]P. Langevin, Ann. Chim. Phys. **5**, 245 (1905).

[62]G. Gioumousis and D. P. Stevenson, The Journal of Chemical Physics **29**, 294 (2004).

[63]R. Feistel and W. Wagner, Geochimica et Cosmochimica Acta **71**, 36 (2007).

[64]T. F. Magnera, D. E. David, D. Stulik, R. G. Orth, H. T. Jonkman, and J. Michl, Journal of the American Chemical Society **111**, 5036 (1989).